Conserved and Cooperative Assembly of Membrane-Bound α-Helical States of Islet Amyloid Polypeptide[†]

Jefferson D. Knight,[‡] James A. Hebda,[§] and Andrew D. Miranker*,[§]

Department of Pharmacology and Department of Molecular Biophysics and Biochemistry, Yale University,
260 Whitney Avenue, New Haven, Connecticut 06520-8114

ABSTRACT: The conversion of soluble protein into β-sheet-rich amyloid fibers is the hallmark of a number of serious diseases. Precursors for many of these systems (e.g., Aβ from Alzheimer's disease) reside in close association with a biological membrane. Membrane bilayers are reported to accelerate the rate of amyloid assembly. Furthermore, membrane permeabilization by amyloidogenic peptides can lead to toxicity. Given the β-sheet-rich nature of mature amyloid, it is seemingly paradoxical that many precursors are either intrinsically α-helical or transiently adopt an α-helical state upon association with membrane. In this work, we investigate these phenomena in islet amyloid polypeptide (IAPP). IAPP is a 37-residue peptide hormone which forms amyloid fibers in individuals with type II diabetes. Fiber formation by human IAPP (hIAPP) is markedly accelerated by lipid bilayers despite adopting an α-helical state on the membrane. We further show that IAPP partitions into monomeric and oligomeric helical assemblies. Importantly, it is this latter state which most strongly correlates to both membrane leakage and accelerated fiber formation. A sequence variant of IAPP from rodents (rIAPP) does not form fibers and is reputed not to permeabilize membranes. Here, we report that rIAPP is capable of permeabilizing membranes under conditions that permit rIAPP membrane binding. Sequence and spectroscopic comparisons of rIAPP and hIAPP enable us to propose a general mechanism for the helical acceleration of amyloid formation in vitro. As rIAPP cannot form amyloid fibers, our results show that fiber formation need not be directly coupled to toxicity.

Amyloid formation is a major component of degenerative processes in a number of serious diseases, including Alzheimer's disease and type II diabetes (*2*, *4*). In each disease, a characteristic precursor protein assembles into highly ordered β-sheet-rich fibers. Amyloid fibers are characterized by a cross-β structure, in which individual β-strands are oriented orthogonal to the long fiber axis. The β-sheets, which are parallel to the long fiber axis, are typically composed of parallel rather than antiparallel strands (*5−8*). In most amyloid diseases, the presence of amyloid is closely correlated with the extent of disease progression, which suggests that amyloid formation may contribute to degenerative processes such as cell death.

The association of amyloid with cell death is supported by the observation that soluble oligomeric states of amyloidogenic proteins induce disease-like toxicity when added to cultured cells (*4*, *9*) or injected into rats (*10*). These same states have been observed to render synthetic lipid membranes permeable in vitro. This has led to the hypothesis that membrane disruption by oligomeric states, through either pore formation or detergent-like effects, is a general mechanism of cytotoxicity in amyloid diseases (*4*, *11*). Interestingly, a large number of disease-associated amyloidogenic proteins reside in close proximity to the membrane in vivo. These include amyloid proteins from Alzheimer's disease (Aβ) (*12*), prion disease (PrP) (*13*), and Parkinson's disease (α-synuclein) (*14*). The amyloid protein from type II diabetes, islet amyloid polypeptide (IAPP,[1] also known as amylin), resides within a narrow volume near the membrane of insulin secretory granules (*3*). The cytotoxic structures of these proteins, their relation to amyloid fiber formation, and the mechanism of toxicity are not well understood. A more thorough knowledge of the mechanisms of membrane interaction and amyloid fiber formation is central to understanding the progression of all amyloid diseases.

IAPP is the protein component of amyloid in type II diabetes. IAPP is a 37-residue peptide normally processed

---

* To whom correspondence should be addressed. E-mail: andrew.miranker@yale.edu. Voice: (203) 432-8954. Fax: (203) 432-5175.
‡ Department of Pharmacology, Yale University.
§ Department of Molecular Biophysics and Biochemistry, Yale University.

[1] Abbreviations: IAPP, islet amyloid polypeptide (amylin); hIAPP, human IAPP; rIAPP, rat/mouse IAPP; DOPG, 1,2-dioleoyl-*sn*-glycero-3-(phospho-*rac*-1-glycerol); DOPC, 1,2-dioleoyl-*sn*-glycero-3-phosphocholine; DOPS, 1,2-dioleoyl-*sn*-glycero-3-phosphoserine; DMSO, dimethyl sulfoxide; ThT, thioflavin T; HFIP, 1,1,1,3,3,3-hexafluoro-2-propanol; CD, circular dichroism; UV, ultraviolet; P/L, molar ratio of protein to lipid; CT, ratio of total protein on membrane to lipid; C_m, ratio of monomeric protein on membrane to lipid; C_{agg}, ratio of aggregated protein on membrane to lipid; CT_{max}, maximum total protein to lipid ratio on membrane; FL, fraction of liposomes leaked at any given time; SVD, singular value decomposition.
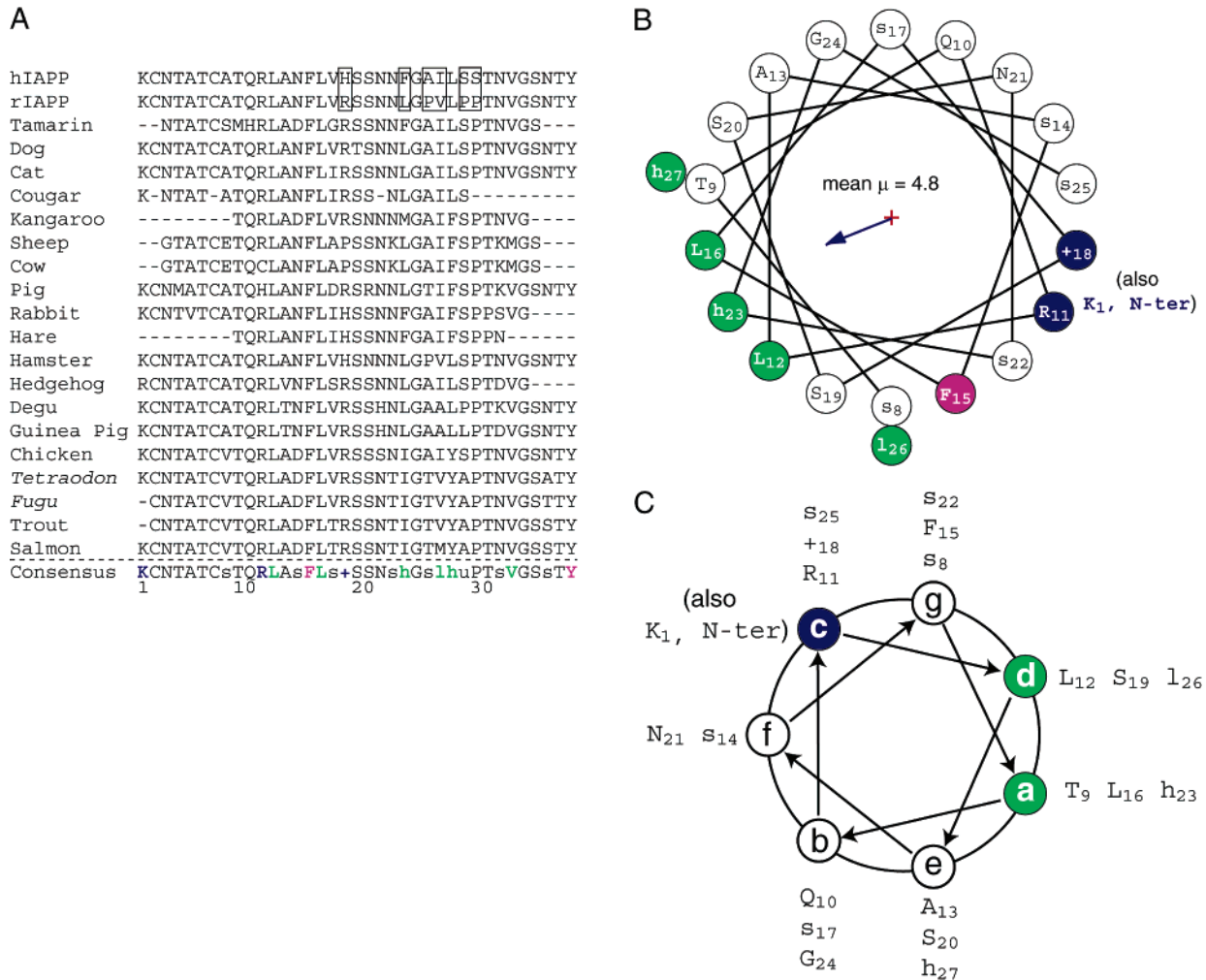
FIGURE 1: Amino acid sequence analysis of IAPP. (A) Multiple sequence alignment including human (hIAPP, line 1), rat/mouse IAPP (rIAPP, line 2), and 80% consensus among 21 known sequences (bottom). Boxes indicate positions at which hIAPP and rIAPP differ. Dashes indicate unknown amino acids. Key to consensus sequence: s = small, + = positive, h = hydrophobic, l = aliphatic, u = tiny. All peptides contain disulfide bonds between residues 2 and 7 and are C-terminally amidated. (B) Helical wheel representation created using MPEx (*44*). The consensus sequence shows a conserved hydrophobic moment, as well as alignment of cationic residues on the same side of the helix. Green circles indicate hydrophobic residues, blue indicate basic residues, and violet indicate aromatic residues. The hydrophobic moment from each sequence is in the direction of residue 16 or 23 and has a value of 4.8 ± 0.5. (C) Alignment of consensus sequence on a heptad shows two adjacent leucine-rich positions (positions a and d), consistent with a coiled-coil helix association motif.

and cosecreted with insulin by the β cells of the islets of Langerhans. In late stages of diabetes, β-cell mass decreases due to cell death, and IAPP amyloid is observed in ~90% of cases post-mortem (*15*). By contrast, the rat/mouse variant (rIAPP) cannot form amyloid although it differs at only 6 out of 37 amino acid positions (Figure 1A). Notably, rat and mouse models of diabetes require genetic alteration of lipid metabolism and/or extremely high fat diet (*16*, *17*). While β-cell death is less frequent in diabetic rodents than humans, this phenomenon has been observed in Zucker diabetic fatty rats as well as in isolated mouse islets (*18*, *19*). Furthermore, rodent β-cell function becomes impaired in early diabetes by an unknown mechanism (*20*). One important observation is that transgenic rats or mice expressing human IAPP (hIAPP) become strongly predisposed to diabetes and have higher rates of β-cell apoptosis (*21*, *22*). This suggests that hIAPP is an important factor for β-cell toxicity in type II diabetes.

In vitro, IAPP forms ordered structures on lipid membranes. IAPP−lipid binding is strongly dependent on anionic lipid charge (*23*, *24*). Notably, anionic phospholipid levels in islets increase significantly following glucose stimulation (*24*, *25*). While the initial IAPP structures formed upon membrane binding are α-helical (*26*), membrane binding accelerates formation of β-sheet amyloid fibers by hIAPP (*23*). Several other natively unfolded amyloid precursors, including Aβ and α-synuclein, also form α-helical structures upon association with lipid bilayers (*27*, *28*). In addition, solvents that promote helical structure accelerate fibrillization of these proteins (*29−31*), and an α-helical intermediate state has been observed on the pathway for Aβ fiber formation in solution (*32*). It is seemingly paradoxical that stabilization of helical conformations accelerates the formation of β-sheet-rich amyloid. A better understanding of the aggregation propensity of α-helical membrane-bound hIAPP will help to elucidate why these events appear to catalyze amyloid fiber formation. The aim of this study is to investigate the thermodynamic and structural mechanisms of IAPP−membrane interactions. These interactions have important implications both in the context of type II diabetes and for native physiological functions of IAPP.

MATERIALS AND METHODS

Materials. DOPG was obtained from Avanti (Alabaster, AL) dissolved in chloroform; DMSO was from J. T. Baker; thioflavin T (ThT) was from Acros; calcein, glutaraldehyde, and 1,1,1,3,3,3-hexafluoro-2-propanol (HFIP) were from Sigma. hIAPP was synthesized using standard t-Boc methods and purified by the W. M. Keck facility (New Haven, CT). rIAPP was synthesized using Fmoc methods and cyclized and purified in house.
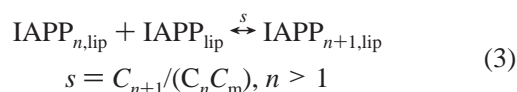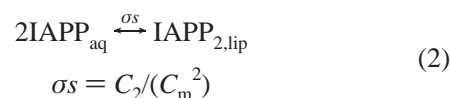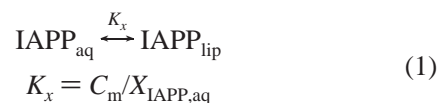
IAPP, Liposome, and Buffer Stock Preparation. After purification, rIAPP was lyophilized, solubilized with water, and filtered through a 0.22 μm Tuffryn syringe filter. hIAPP stocks for fiber formation kinetics and liposome leakage assays were prepared in DMSO as previously described (*23*). For CD experiments, hIAPP was lyophilized from a stock in HFIP (*29*), solubilized in water, and filtered through a 0.22 μm Tuffryn syringe filter. Stocks were kept on ice for the duration of CD experiments (<10 h). IAPP stock concentrations were determined by UV absorbance, using $\epsilon_{280} = 1400$ mol^{-1} cm^{-1}. For CD, stock concentrations were approximately 300 μM (hIAPP) or 900 μM (rIAPP). DOPG concentrations are reported as dilutions from a 10.0 mg/mL stock as determined by the mass of dried lipid prior to suspension in buffer (FW = 797 g/mol). Liposomes were prepared by extrusion through 100 or 220 nm polycarbonate filters, as previously described (*23*). Lipid loss from this procedure is consistently 12 ± 4%. Unless otherwise noted, all experiments were performed at 25 °C in phosphate buffer (50 mM potassium phosphate, 100 mM KCl, pH 7.4). Data shown in each figure panel are of representative measurements using one stock of IAPP. All reported trends have been reproduced in at least three independent experiments with different peptide stocks.

CD Spectroscopy. Circular dichroism measurements were taken on an Aviv 215 spectrometer (Aviv Associates, Lakewood, NJ) using 1 or 2 mm path length cuvettes. Spectra of liposomes in buffer were subtracted for each lipid concentration used. For hIAPP kinetics, spectra (200−260 nm) were measured every 1 nm with 5 s averaging time and denoised using singular value decomposition (SVD). For secondary structure estimation, spectra (200−260 nm) were measured every 1 nm with 15 s averaging time.

For IAPP−lipid binding measurements, concentrated DOPG liposomes were titrated into IAPP in the cuvette. For rIAPP, full spectra (211−260 nm) were obtained at each protein and lipid concentration (1 nm per point, 5 s averaging time) and denoised using SVD (two basis spectra) before extracting θ_{222}. For hIAPP, it was necessary to complete each titration within the lag time of fiber formation. Therefore, only ellipticity at 222 nm and baseline (260 nm) were measured two to four times (10 s averaging time) for each protein and lipid concentration. Each titration was concluded within 30 min. At the end of each titration, a full spectrum was recorded to verify that the protein had not yet converted to β-sheet. Each displayed dual minima at 222 and 208 nm, indicative of α-helical structure (*33*). The helical content is constant during the lag time of fiber formation, during which the titrations were performed. Secondary structure was estimated from CD spectra using the SEL-CON3, CONTINLL, and CDSSTR algorithms within CDPro (*34*). A basis set of spectra was used (reference set SMP56)

(*35*), which is taken from 43 soluble and 13 membrane proteins.

Global Data Analysis. Data analysis of lipid binding was performed using Mathematica (Wolfram Research). Global analysis of binding data was performed using two thermodynamic models, which we term "heterogeneous aggregation" and "discrete oligomerization". The heterogeneous aggregation model was originally developed by Terzi and Seelig and adapted for membrane binding by Wimley and White (*36*, *37*). The limit of this model at infinite peptide dilution is one described simply by partitioning into the membrane with a molar partition coefficient K_x ("simple partitioning" model). At higher peptide concentration, monomers partition into the membrane and aggregate reversibly in the membrane phase with equilibria described by a nucleation parameter σ and a propagation parameter s:

$$\text{IAPP}_{\text{aq}} \overset{K_x}{\rightleftharpoons} \text{IAPP}_{\text{lip}}$$
$$K_x = C_{\text{m}}/X_{\text{IAPP,aq}} \tag{1}$$

$$2\text{IAPP}_{\text{aq}} \overset{\sigma s}{\rightleftharpoons} \text{IAPP}_{2,\text{lip}}$$
$$\sigma s = C_2/(C_{\text{m}}^2) \tag{2}$$

$$\text{IAPP}_{n,\text{lip}} + \text{IAPP}_{\text{lip}} \overset{s}{\leftrightarrow} \text{IAPP}_{n+1,\text{lip}}$$
$$s = C_{n+1}/(C_n C_{\text{m}}), \; n > 1 \tag{3}$$

Here, C_{m} and C_n are the mole fraction concentrations of monomeric and n-meric lipid-bound IAPP, respectively [approximated as molar ratio of peptide to lipid (P/L)] and $X_{\text{IAPP,aq}}$ is the mole fraction concentration of IAPP in solution, given by

$$X_{\text{IAPP,aq}} = [\text{IAPP}]_{\text{aq}}/[\text{H}_2\text{O}] \tag{4}$$

The total concentration of IAPP on the membrane in monomer units (CT) is given by

$$\text{CT} = C_{\text{m}}\left(1 - \sigma + \frac{\sigma}{(1 - sC_{\text{m}})^2}\right) \tag{5}$$

The equation used for the global fit was generated by solving eqs 1 and 5, along with the conservation-of-peptide equation:

$$[\text{IAPP}]_{\text{total}} = X_{\text{IAPP,aq}}[\text{H}_2\text{O}] + \text{CT}[\text{DOPG}]_{\text{total}} \tag{6}$$

for CT as a function of $[\text{IAPP}]_{\text{total}}$ and $[\text{DOPG}]_{\text{total}}$ and then making the following modifications. (i) To account for saturation of peptide on the membrane, we defined a revised CT (CT*) which is equivalent to CT at low P/L but approaches a maximum concentration (CT$_{\text{max}}$), hyperbolically as the predicted CT increases:

$$\frac{(\text{CT} - \text{CT*})(\text{CT}_{\text{max}} - \text{CT*})}{\text{CT*}} = \lambda \tag{7}$$

The hyperbolic transition constant λ determines the steepness with which CT* approaches CT and CT$_{\text{max}}$, and is here arbitrarily set to 0.005. (ii) CT* was converted to a molar residue ellipticity at 222 nm ($[\theta]_{222}$) by the

following conversion:

$$[\theta]_{222} = [\theta]_{222,0} + ([\theta]_{222,\text{lim}} - [\theta]_{222,0})\text{CT}^*[\text{DOPG}]_{\text{total}}/[\text{IAPP}]_{\text{total}} \quad (8)$$

where $[\theta]_{222,0}$ is the molar residue ellipticity of aqueous peptide and $[\theta]_{222,\text{lim}}$ is the molar residue ellipticity when 100% bound to membrane.

The fitting routine optimized the six parameters ($[\theta]_{222,0}$, $[\theta]_{222,\text{lim}}$, K_x, σ, s, and CT_{max}) to best fit the experimentally measured $[\theta]_{222}$ as a function of $[\text{DOPG}]_{\text{total}}$ and $[\text{IAPP}]_{\text{total}}$. Error analysis was performed using Monte Carlo analysis with per point errors estimated from the average residuals of each titration.

The discrete oligomerization model involves partitioning (eq 1) followed by formation of oligomers of size N:

$$N\text{APP}_{\text{lip}} \xleftarrow{K_{\text{olig}}} \text{IAPP}_{N,\text{lip}}$$
$$K_{\text{olig}} = C_N/(C_{\text{m}})^N \quad (9)$$
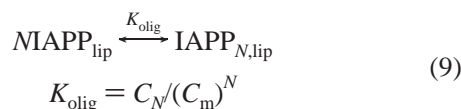
In this case, CT is given by

$$\text{CT} = C_{\text{m}} + (NK_{\text{olig}}C_{\text{m}}^{N}) \quad (10)$$

Equations 1, 6, and 10 were solved for CT, and the modifications of eqs 7 and 8 were applied. Fitting was performed with N restricted to integer values. Both the discrete oligomerization and heterogeneous aggregation models assume that the available membrane surface is independent of peptide concentration.

Liposome Aggregation Measurements. Light scatter measurements were performed using a Perkin-Elmer Lambda 25 spectrophotometer with a 1 cm cell. Titrations of DOPG into IAPP were performed as described for CD spectroscopy. For each addition, plateau values of absorbance at 350 nm are reported as measured after 2 min (hIAPP) or 5 min (rIAPP).

Cross-Linking. Cross-linking was initiated by addition of 0.01% (10 μM) glutaraldehyde to rIAPP and DOPG mixtures which had been preincubated for 10 min. Reactions were quenched after 40 min by addition of 100 mM D-lysine. Separation was performed by SDS−PAGE using 17% acrylamide gels and the Tris−tricine buffer system (38). Gels were fixed with 1% glutaraldehyde and silver stained.

Measurement of hIAPP Fiber Formation Kinetics by ThT Fluorescence. Fiber formation reactions were initiated by dilution of hIAPP stocks into phosphate buffer with 50 μM ThT and monitored by fluorescence (excitation 450 nm, emission 486 nm) in a FluoDia T70 fluorescence plate reader (PTI, London, Ontario, Canada). Measurements were made without agitation. Background fluorescence of ThT and lipid alone was subtracted from each data point prior to curve fitting. Fitting of kinetic data and extraction of t_{TM} were performed as described previously (23). Briefly, reaction time courses were fit to sigmoid curves of the form

$$I = \frac{(b_1 + m_1 t) + (b_2 + m_2 t)e^{(t_{50}-t)/\tau}}{1 + e^{(t_{50}-t)/\tau}} \quad (11)$$

Values of t_{TM} are reported as the time at which the slope of this curve is maximal.

Liposome Leakage Assay. DOPG vesicles containing 30 mM calcein were prepared in a Tris−KCl buffer with the same pH and ionic strength as the phosphate buffer used above (50 mM Tris, 124 mM KCl, pH 7.4). Liposomes were separated from free dye by size exclusion chromatography, and lipid concentration was determined by total phosphorus measurement (39). Concentrated liposomes were added to solutions of peptide or Triton X-100 in phosphate buffer and immediately transferred into fluorescence cuvettes. Fluorescence intensity (excitation 485 nm, emission 500 nm) was monitored using a PTI QuantaMaster C-61 fluorescence spectrophotometer (PTI, London, Ontario, Canada) and is expressed as fractional intensity increase relative to that induced by 0.004% Triton X-100. The resultant time courses fit well to curves of the form

$$\text{FL}_t = (\text{FL}_0 - \text{FL}_{\text{max}})e^{-kt} + \text{FL}_{\text{max}} \quad (12)$$

where FL_t is the fractional leakage at time t. For comparison with previous reports of similar experiments, the fractional leakage at 10 min is interpolated from the fit (40, 41). CD binding assays using liposome stocks prepared in Tris−KCl buffer and diluted into phosphate buffer demonstrated that IAPP−DOPG binding under these conditions is identical to that in phosphate buffer (data not shown).

Sequence Alignment and MPEx Analysis. IAPP protein sequences were obtained from a FASTA search using hIAPP as the input sequence, with the addition of reported sequences from *Fugu rubripes*, *Oncorhynchus mykiss*, and *Salmo salar* (42). Alignment and consensus were determined manually using the default annotation defined by MView (43). Helical wheel alignment was performed using MPEx (44), using input sequences containing residues 8−27. Histidine and aspartate residues were assumed to be charged; glutamate (residue 8 in cow and sheep) was input as neutral.

RESULTS

Our goals in this work are to gain structural insights into conformational states of IAPP on membrane surfaces and to relate these structures to fiber formation and membrane permeabilization. Our approaches use optical spectroscopy to make thermodynamic and structural measurements during the lag phase of fiber assembly. Specifically, circular dichroism spectroscopy (CD) is used to measure binding affinity and the membrane-bound structure of IAPP. Relating these structures to amyloid formation is achieved by kinetic measurement of fiber assembly using fluorescence and CD. In addition, leakage of fluorescent dye from liposomes allows us to measure the effects of preamyloid structures on bilayer stability. Of particular importance in this work are comparisons of hIAPP to rIAPP (Figure 1A). For clarity, we use the abbreviations hIAPP and rIAPP to refer to properties of each variant and IAPP to refer to properties measured or proposed to be common between the two. As rIAPP binds membranes, but does not assemble into amyloid, it allows us to investigate membrane-bound states in the context of the amyloid formation pathway.

CD Spectroscopy of IAPP and Liposomes. IAPP is random coil in solution but initially forms α-helical structures upon binding to DOPG liposomes (Figure 2A). The presence of α-helical structure is most evident in hIAPP as two canonical minima are present at 208 and 222 nm. rIAPP has a
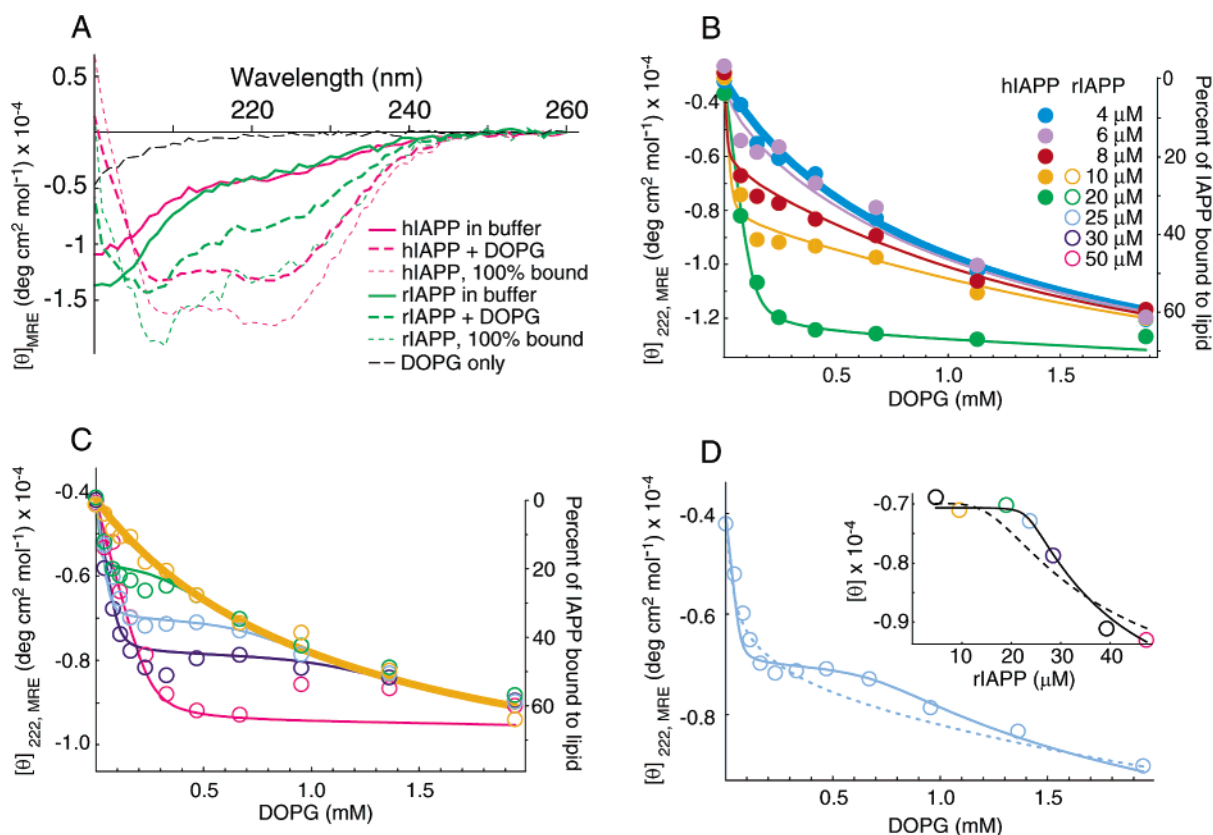
FIGURE 2: Far-UV CD of IAPP binding to liposomes. (A) Spectra of 20 μM rIAPP (green) or hIAPP (magenta) were measured in phosphate buffer (solid lines) and in the presence of 1.3 mM DOPG (thick dashes). IAPP spectra shown are difference spectra between samples with and without peptide. For reference, the spectrum of 1.3 mM DOPG alone is shown (dashed black line), which does not interfere with peptide measurement. On the basis of the calculated fraction of IAPP bound at these concentrations, the spectrum of 100% bound peptide was determined (thin dashes). (B–D) Protein–membrane binding curves for (B) hIAPP and (C, D) rIAPP. DOPG liposomes were titrated into the indicated total concentration of peptide, and the ellipticity at 222 nm was measured. Cooperativity is apparent in that higher concentrations of peptide require less lipid for binding. Global analyses using six parameters were performed using 40 (hIAPP) or 72 (rIAPP) data points. Curves shown are derived from models in which partitioning is followed by discrete oligomerization [dashed lines in (D)] or heterogeneous aggregation [solid lines (B–D)]. (D) Curves from both models are shown for the titration at 25 μM rIAPP. Inset: Ellipticity is plotted as a function of rIAPP concentration at 0.67 mM DOPG. This lipid concentration is within the apparent plateau region in the titrations shown in (C). The right axis (B, C) shows the percentage of bound protein, as determined from the heterogeneous aggregation model. For clarity, only five of seven rIAPP titrations are shown in (C). Heavy lines in (B) and (C) represent protein concentrations at which partitioning dominates binding.

diminished ellipticity at 222 nm relative to human but a strong minimum at 207 nm indicative of α-helix. From these data, the total extent of helicity is estimated as 39–43% for hIAPP and 32–36% for rIAPP, when 20 μM peptide and 1.3 mM DOPG are present (*34*). Similar estimates of helical structure have been reported recently for hIAPP binding to anionic DOPS (*26*), suggesting that α-helical binding is charge dependent but not headgroup specific. By contrast, we estimate the helical content in buffer alone to be only ~10% for both peptides. The estimated β-sheet content for both peptides is ~30% in buffer and 10–15% in the presence of lipid. As CD is an ensemble technique, the spectrum measured in the presence of lipid is the population average of membrane-bound and solution states. The lower helical content of rIAPP in the presence of lipid may be due in part to its lower affinity for membranes (*23*). Therefore, an accurate measurement of helicity per bound IAPP molecule requires quantitative measurement of IAPP–lipid binding.

Binding of hIAPP and rIAPP to DOPG membranes is cooperative, driven by both protein–membrane and protein–protein contacts. Using CD ellipticity at 222 nm as a measurement of membrane binding, we performed titrations of DOPG into rIAPP or hIAPP, ensuring that measurements

were complete within the lag time of fiber formation for hIAPP. At low protein concentrations, both hIAPP ($\leq$4 μM) and rIAPP ($\leq$10 μM) binding to DOPG can be fit by a model in which IAPP simply partitions between the aqueous phase and the membrane bilayer [Figure 2B,C (heavy curves)]. The mole fraction partition coefficient (K_x), or equilibrium constant, for this transition is $4.9 \times 10^4 \pm 0.5 \times 10^4$ and $4.9 \times 10^4 \pm 0.6 \times 10^4$ for hIAPP and rIAPP, respectively (Table 1). This corresponds to phospholipid dissociation constants of roughly 1 mM for both peptides (*45*), which is comparable to the concentration of IAPP in the halo region of the secretory granule (0.8–4 mM).[2] This simple partitioning model assumes that binding affinity is independent of the total peptide concentration. However, we observe that as protein concentration is raised, the binding affinity clearly increases. For example, considerably less DOPG is required to achieve saturation of binding at 20 μM hIAPP (Figure 2B, green) compared to 4 μM (Figure 2B, blue). Cooperat-

Table 1: Parameters Derived from Heterogeneous Aggregation Model of Cooperative Binding

	hIAPP−DOPG	rIAPP−DOPG
K_x	49000 ± 5000^a	49000 ± 6000
σ	0.04 ± 0.03	0.001 ± 0.004
s	180 ± 12	73 ± 6
CT_{max}	0.09 ± 0.01	0.12 ± 0.01
$[\theta]_{222,0}$ (deg cm^2 mol^{-1})	-3200 ± 200	-4200 ± 100
$[\theta]_{222,lim}$ (deg cm^2 mol^{-1})	-18000 ± 1000	-12000 ± 1000
$\Delta G°_{part} = -RT \ln(K_x)$ (kcal/mol)	-6.4 ± 0.1	-6.4 ± 0.1
$\Delta G°_{nuc} = -RT \ln(s\sigma)$ (kcal/mol)	-0.9 ± 0.6	$\geq +0.5$
$\Delta G°_{prop} = -RT \ln(s)$ (kcal/mol)	-3.1 ± 0.1	-2.5 ± 0.1

^{a} Confidence intervals represent one standard deviation as estimated by Monte Carlo error analysis. Note: this method underestimates error in $\Delta G°_{part}$, which varies by ≤ 0.5 kcal/mol in repeat experiments with different peptide stocks.

ivity in binding is most readily explained by the presence of protein−protein interactions on the membrane.

Direct Detection of Membrane-Bound Associations. IAPP interaction on the membrane is the simplest explanation for the cooperative binding profiles observed by CD. However, we also considered the alternate possibility that cooperative binding is driven by IAPP-induced liposome aggregation, which has been reported previously (*46*). Upon addition of DOPG liposomes to rIAPP or hIAPP, increased light scatter at 350 nm is detected only at IAPP concentrations ≥ 30 μM for both hIAPP and rIAPP (Figure 3A,B). In contrast, cooperative binding occurs at concentrations ≥ 6 μM hIAPP and 20 μM rIAPP (Figure 2B,C). Furthermore, the binding curve of 25 μM rIAPP measured by CD is identically cooperative whether 100 or 220 nm extruded liposomes are used (Figure 3B, inset). This occurs despite the ∼5-fold difference in the molar concentration of liposomes at the same total DOPG concentration. If cooperativity were driven by liposome aggregation, one would expect it to be dependent on the molar concentration of liposomes. Our observations suggest that liposome aggregation is a consequence of α-helical IAPP assembly on the membrane.

The presence of membrane-bound rIAPP aggregates is directly detectable using glutaraldehyde cross-linking. Glutaraldehyde cross-links proteins by reacting with lysine side chains and other moieties (*47*). Figure 3C shows that cross-linked oligomers as large as hexamers are formed when 25 μM rIAPP is cooperatively bound to the membrane (e.g., 125 μM DOPG). At higher lipid concentrations, e.g., 1.5 mM, cross-linked dimers are formed efficiently, but higher order species are not. This decrease in higher order cross-linking correlates with the convergence of the 25 μM rIAPP binding curve with simple partitioning at concentrations of DOPG above ∼1 mM (Figure 2C). At high lipid concentrations (Figure 3C, far right lane), dimers are the most efficiently formed cross-linked species with little contribution from larger states. However, this may represent simple enhancement of the weak degree of cross-linking observed in the absence of lipid (Figure 3C, far left lane). Thus, only under conditions where rIAPP is cooperatively bound is a range of higher order oligomers observed.

Global Analysis of Cooperative IAPP−Lipid Binding. The observation of a range of species via chemical cross-linking suggests that cooperativity is not the result of the formation of a discretely sized membrane-bound oligomer. Global
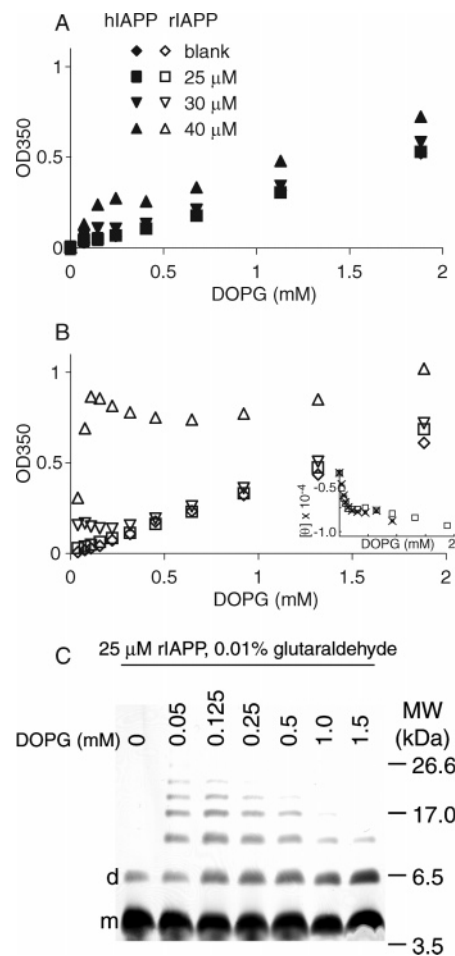

FIGURE 3: Direct measurement of aggregation upon IAPP−liposome binding. (A, B) Aggregation of liposomes induced by hIAPP or rIAPP, respectively. DOPG liposomes were titrated into the indicated starting concentrations of IAPP, and the extent of light scatter was measured by absorbance at 350 nm. Inset to (B): CD titrations of 100 nm (squares) or 220 nm ($\times$) DOPG liposomes into 25 μM rIAPP. Light scatter obscures ellipticity measurements with the larger liposomes above 1 mM DOPG. (C) Glutaraldehyde cross-linking of rIAPP + DOPG. rIAPP (25 μM) was incubated for 40 min with 0.01% glutaraldehyde and the indicated concentration of DOPG liposomes (100 nm). Reactions were quenched prior to separation by SDS−PAGE. The positions of molecular weight markers are shown on the right, and monomer (m) and dimer (d) bands of rIAPP are indicated on the left.

analysis of the CD titration data (Figure 2B,C) was performed with a discrete oligomerization model, in which IAPP partitioning is followed by formation of oligomers of size N. Global analysis is a more stringent test of a model than individual curve fitting, as it requires measurements from multiple data sets to be represented by a small number of parameters. Global fits using the six-parameter discrete oligomerization model generally improve as N increases but do not change significantly above $N = 7$ (Figure 2D, $N = 7$ shown). Correlation of these fits with the data is poor and delivers nonrandom residuals. For example, at 25 μM rIAPP (Figure 2D), ellipticity approaches an apparent plateau between 0.2 and 0.7 mM DOPG but then becomes more negative at higher lipid concentrations. A plateau within a titration curve generally suggests a change of state. Such behavior cannot be captured by an equilibrium between monomer and an oligomer of discrete size (Figure 2D, dashed line). Indeed, this model consistently fails to account for

ellipticity throughout these plateau regions, e.g., 20–40 μM rIAPP, 0.67 mM DOPG (Figure 2D, inset, dashed line).

In contrast, binding is well represented by a model in which an equilibrium exists between heterogeneous aggregates and monomeric forms of IAPP on the membrane. In this model, α-helical IAPP assembles on the membrane into multimeric species of heterogeneous size via nucleation-dependent aggregation. This model has been previously used to describe cooperative membrane binding by the peptide sequence Ac-WLLLLL (37). Importantly, this model contains the same number of fitting parameters (6) as the discrete oligomerization model above, with the oligomer size, N, and equilibrium constant, K_{olig}, replaced by an aggregate nucleation parameter, σ, and propagation parameter, s. This heterogeneous aggregation model yields robust fits to data from both hIAPP (Figure 2B, $R^2 = 0.99$) and rIAPP (Figure 2C, $R^2 = 0.96$), including capture of the apparent plateau of ellipticity (Figure 2D, solid lines). As this is an equilibrium thermodynamic model, it does not preclude the existence of low population intermediate states, e.g., oligomers in solution. We note, however, that IAPP is predominantly unstructured in solution, which would give rise to comparatively weak associations. Furthermore, rIAPP has not been reported to form oligomers in solution. Thus, the simplest interpretation of these data is that IAPP aggregation occurs on the membrane. In either case, global analysis clearly indicates that cooperative IAPP–membrane binding is due to formation of heterogeneous α-helical aggregates rather than discrete oligomers.

The formation of membrane-bound α-helical aggregates is itself a cooperative process. The heterogeneous aggregation model reports an aggregate propagation parameter, s, which is the equilibrium constant for addition of monomer to an aggregate. This value is 180 ± 12 for hIAPP and 73 ± 6 for rIAPP, reflecting a ~2.5-fold increased preference for the aggregated state in hIAPP relative to rIAPP. The model also includes an aggregate nucleation parameter, σ, which has a value between 0 and 1. This value scales the propagation parameter s only for the assembly that corresponds to nucleation, i.e., the product, σs, corresponds to the equilibrium constant for nucleation of aggregates. The best-fit values of σ (0.04 ± 0.03 for hIAPP, 0.001 ± 0.004 for rIAPP) imply a highly cooperative aggregation. For simplicity, we assume this step is dimer formation; however, our data do not exclude the possibility of a larger nucleus size. In addition to σ, s, and the monomer partitioning coefficient, K_x, the fits also report the maximum protein to lipid ratio (P/L) of IAPP on the membrane (CT_{max}), which is approximately 1/8 for both variants (Table 1). When the overall P/L approaches this value, IAPP is overwhelmingly in the aggregated state. It is important to note that the aggregates observed here are α-helical and not amyloid fibers, which are β-sheet in structure and do not form from rIAPP. For clarity, we use the term "aggregate" in this work solely to describe this multimeric helical state and do not use it to describe amyloid fibers.

hIAPP Amyloid Fiber Formation. Conversion of α-helical membrane-bound hIAPP species into amyloid fibers involves a transition in secondary structure to β-sheet. Despite the stabilization of α-helix during the lag phase, hIAPP fiber formation is dramatically accelerated by binding to lipid (23). Here, a reaction with 20 μM hIAPP and 0.34 mM DOPG was measured by CD spectroscopy (Figure 4A,B). After an initial lag phase (in this case ~60 min), a cooperative loss of helical structure and acquisition of β-sheet are evident. The time scale is consistent with measurements of fiber formation by thioflavin T (ThT) or intrinsic tyrosine fluorescence (data not shown) (23). Singular value decomposition analysis of the CD spectra indicates a two-state transition; i.e., no significant intermediate structure is populated during the transition. No acquisition of β-sheet structure by membrane-bound rIAPP was observed, consistent with its behavior in solution (48). Thus, although rIAPP can form α-helical aggregates when bound to membranes, it cannot undergo a structural conversion to amyloid.

Kinetics of fiber formation by hIAPP are correlated with the concentration of α-helical aggregates. To elucidate which state of membrane-bound hIAPP is preferred for fiber nucleation, we measured fiber formation kinetics of 10 μM hIAPP in the presence of 1–8 mM DOPG. We report the rate of fiber formation by the time at the midpoint of the fiber formation transition (t_{TM}). In agreement with our previous results, only a ~2-fold increase in t_{TM} was observed between 1 and 4 mM DOPG (23). However, the t_{TM} increases dramatically above 4 mM DOPG (Figure 4C). It is expected that t_{TM} should increase (i.e., the rate of fiber formation should decrease) as the concentration of hIAPP on the membrane decreases. As the amount of lipid is raised, the concentrations of both monomer (C_m) and α-helical aggregate (C_{agg}) on the membrane decrease. However, above 4 mM DOPG, C_{agg} decays to a near zero contribution to the total hIAPP on the membrane (Figure 4D); i.e., the population of helical aggregate is only significant under conditions where fiber formation is rapid. Generally, fiber formation is faster under conditions which favor the formation of nucleating species (49). Thus, these data are consistent with a fiber formation mechanism in which the helical aggregate state is on pathway for fiber nucleation.

Liposome Leakage Measurements. Amyloid fiber formation and bilayer destabilization are distinct processes, which occur on dramatically different time scales. To assess the effect of IAPP on membrane integrity, the leakage of a concentrated fluorescent dye, calcein, from liposomes was measured. In these experiments, fluorescence increase was monitored after adding liposomes to different concentrations of IAPP. Leakage has an exponential kinetic profile and occurs well within the lag time of fiber formation. For example, 10 μM hIAPP forms fibers with lag times between 30 and 70 min in 0.3–1 mM DOPG (Figure 4A,C) but induces leakage from 0.4 mM DOPG within 10 min (Figure 5A, inset). We report the fractional leakage after 10 min incubation (FL_{10}) for consistency with other published observations (40, 41). FL_{10} increases as the total concentration of IAPP is increased (Figure 5A,B). Importantly, 5-fold more rIAPP than hIAPP is generally required to evoke the same extent of leakage (arrows, Figure 5A,B). The amount of IAPP required to induce leakage increases as the total lipid concentration increases. Specifically, the concentrations of both monomeric IAPP (C_m) and helical aggregate (C_{agg}) are correlated with the extent of leakage (Figure 5C,D). However, leakage is much more sensitive to increases in C_{agg} than C_m. For example, a C_m of 0.001 induces very little leakage for either hIAPP or rIAPP. In marked contrast, a C_{agg} (in monomer units) of 0.001 induces 100% leakage
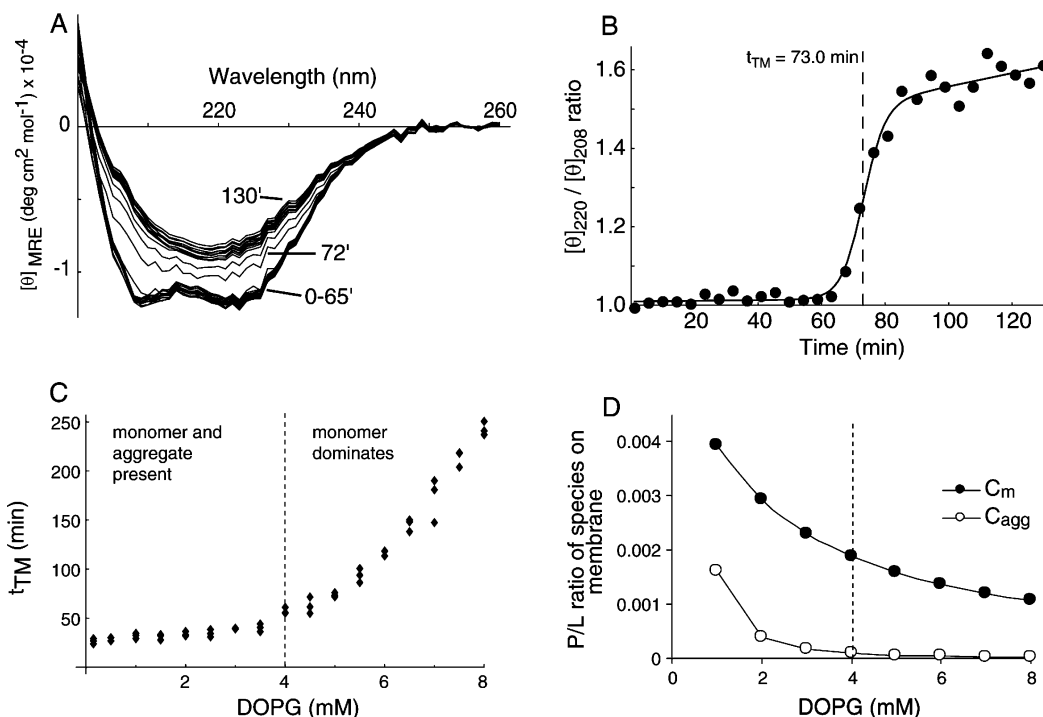
FIGURE 4: hIAPP fiber formation kinetics with DOPG. (A) Far-UV CD spectra of 20 μM hIAPP were measured as a function of time after addition of 0.34 mM DOPG. Spectra were collected every 5 min and were within error of each other between 0 and 65 min. The spectrum at 130 min (130′) has the canonical β-sheet minimum at 220 nm (*33*). (B) The extent of β-sheet content during the reaction is plotted as the ratio of ellipticity at 220−208 nm. The data were fit to a sigmoid curve (solid line) which shows a transition midpoint of 73 min (t_{TM}, dashed line). (C, D) Fiber formation of 10 μM hIAPP was monitored by ThT fluorescence from reactions initiated in parallel using a single stock. Values of t_{TM} were extracted from time courses as described previously (*23*). (C) t_{TM} increases slowly from 1 to 4 mM DOPG but increases dramatically above 4 mM DOPG (indicated by dotted line). (D) The concentrations of membrane-bound monomer (C_m) and helical aggregate (C_{agg}) are plotted versus lipid concentration, as determined from the global fit parameters from Figure 2B. C_{agg} is calculated as CT* − C_m (see Materials and Methods). All concentrations are monomer unit protein to lipid ratios (P/L).

[Figure 5C,D (vertical dashed lines)]. A second indicator is the disparity between hIAPP and rIAPP in the dependence of leakage on monomeric α-helical protein (Figure 5C). These observations suggest it is the α-helical aggregated states of IAPP which most greatly contribute to IAPP-induced membrane disruption.

To our knowledge, this is the first report of membrane disruption by a nonamyloidogenic variant of IAPP. The mechanism of this disruption is not simply due to the mass of protein bound to membrane. rIAPP induces leakage >5-fold more efficiently than the polycationic peptide polylysine, as the latter requires concentrations of ≥0.3 mg/mL to induce the same extent of leakage as 15 μM (0.06 mg/mL) rIAPP (data not shown). Previous reports have shown negligible disruption by rIAPP when the lipid is ≤50% anionic (*9, 40, 50, 51*). Our own observations confirm this result (data not shown). However, these are conditions under which rIAPP does not significantly bind to membranes (*23*). Consistent with a role for aggregates in permeabilization, we find rIAPP induces leakage if it is bound to the membrane under conditions where α-helical aggregates form.

DISCUSSION

IAPP fiber formation and β-cell toxicity are central to the progression of type II diabetes. These two events are correlated clinically, and hIAPP has been implicated in cell death through interactions with cellular membranes. For example, it has been shown that exogenous hIAPP induces

apoptosis in cultured cells under conditions where it also permeabilizes isolated lipid bilayers (*9*). Binding to the membrane also serves to catalyze hIAPP conversion to amyloid fibers (*23*). Here, we elucidate mechanisms for membrane binding, destabilization, and nucleation of fibrillogenesis in vitro using negatively charged liposomes as an analogue for the cellular membrane. Specifically, we find that (i) membrane binding is cooperative; (ii) cooperativity results from formation of a membrane-bound aggregated state; (iii) monomeric and aggregated membrane-bound states are α-helical; (iv) naturally occurring amyloidogenic (human) and nonamyloidogenic (rat) sequence variants bind, fold, and permeabilize bilayers by the same mechanism; (v) fibrillogenesis by hIAPP is nucleated by the cooperative transition of α-helical aggregates into a β-sheet.

The thermodynamic stabilities of IAPP structures on the membrane determine the extent of binding, aggregation, helix-sheet transitions, and membrane permeabilization. Global analysis of binding (Figure 2B−D) is most consistent with a heterogeneous aggregation model in which monomeric IAPP initially partitions from solution into the membrane with a free energy ΔG°_{part} and then aggregates (steps I−III, Figure 6). We can ascribe an overall free energy of IAPP–membrane binding encompassing both partitioning and aggregation steps as

$$\Delta G_{IAPP-mem} = \Delta G^\circ_{part} + f_{Agg}\Delta G_{Agg} \qquad (13)$$

where ΔG°_{part} is the free energy of partitioning at infinite dilution (step I, Figure 6). This is related to the experimen-
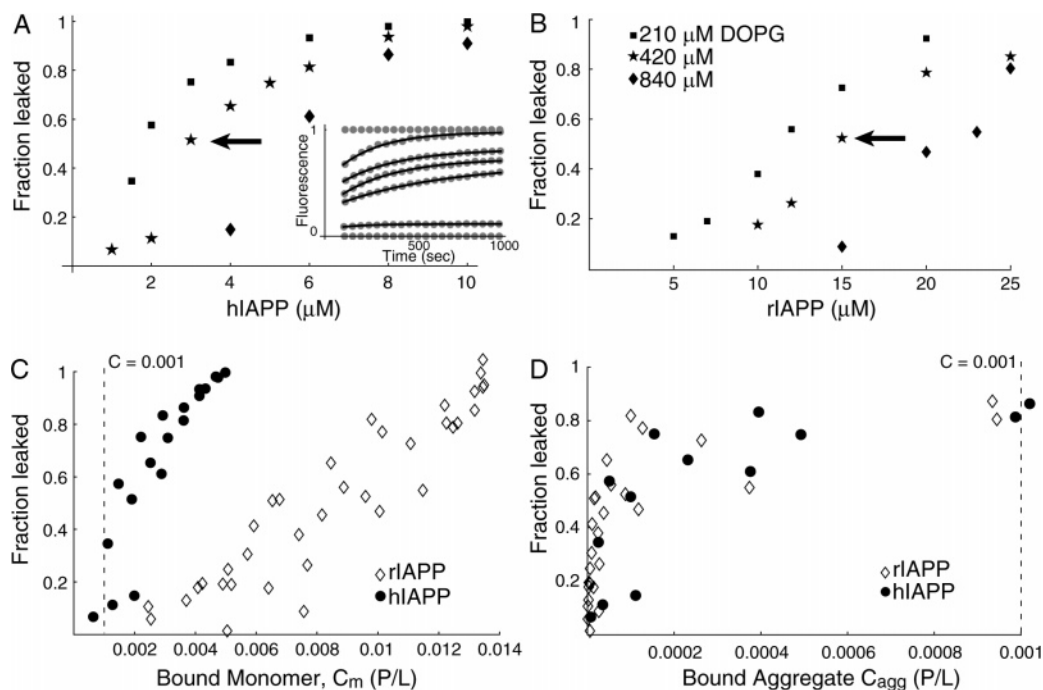
FIGURE 5: Liposome leakage induced by (A) hIAPP and (B) rIAPP. (A, B) Calcein-encapsulating liposomes of 100% DOPG were purified and added to IAPP-containing solutions at total lipid concentrations of 210 μM (squares), 420 μM (stars), or 840 μM (diamonds). Fractional leakage (FL) is reported at 10 min. Arrows indicated that ~50% leakage of 420 μM DOPG is induced by 3 μM hIAPP or 15 μM rIAPP. Complete leakage (FL = 1) was determined from separate solutions containing 0.004% Triton X-100. Inset to (A): Individual leakage time courses fit well to a single exponential with a dead time event and a maximum leakage often less than 100% (shown for 420 μM DOPG and 2−8 μM hIAPP). (C, D) Using the heterogeneous aggregation model, the concentrations of monomeric IAPP on the membrane (C_m) and aggregated α-helical states (C_{agg}) were calculated at each peptide and lipid concentration used. The fraction leakage at 10 min is shown as a function of (C) C_m or (D) C_{agg} for hIAPP (filled circles) and rIAPP (open diamonds). Dashed lines indicate C_m or C_{agg} = 0.001. C_m and C_{agg} are expressed as protein to lipid ratios (P/L).

tally determined mole fraction partition coefficient (K_x) (*45*):

$$\Delta G°_{part} = -RT \ln(K_x) \qquad (14)$$

In eq 13, f_{Agg} is the fraction of membrane-bound protein in the aggregated state and ΔG_{Agg} is the free energy of formation of aggregates. The latter is dependent on aggregate size, as aggregation involves both nucleation and propagation steps (steps II and III, Figure 6). The free energy (per monomer unit) ΔG_{Agg} of forming an aggregate of size N is given by

$$\Delta G_{Agg} = [\Delta G°_{nuc} + (N - 2)\Delta G°_{prop}]/N \qquad (15)$$

Here, $\Delta G°_{nuc}$ is the free energy of aggregate nucleation (step II in Figure 6) and $\Delta G°_{prop}$ is the free energy of adding monomer to an existing aggregate (denoted as propagation; step III in Figure 6).

We interpret our measurement of $\Delta G°_{part}$ using an established approach (*45*) in which the partitioning free energy is represented as a sum of separable contributions:

$$\Delta G°_{part} = \Delta G°_{con} + \Delta G°_{solv} + \\ \Delta G°_{qE} + \Delta G°_{lip} + \Delta G°_{imm} \quad (16)$$

These terms represent energy changes upon protein binding which result from protein folding ($\Delta G°_{con}$), desolvation and nonpolar interactions ($\Delta G°_{solv}$), electrostatic interactions ($\Delta G°_{qE}$), and entropy losses associated with perturbation of lipid structure and immobilization of the protein ($\Delta G°_{lip}$ and $\Delta G°_{imm}$, respectively).

While the values of $\Delta G°_{part}$ are closely similar for rIAPP and hIAPP (−6.4 ± 0.1 kcal/mol for both variants), the contributions of these terms are weighted differently for the two peptides. Previous studies demonstrate that electrostatic interactions ($\Delta G°_{qE}$) greatly contribute to the effectiveness of anionic lipid to catalyze fiber formation. For example, the mutation K1E reduces the acceleration of hIAPP fiber formation by DOPG by ~10-fold (*23*). However, rIAPP has a greater net positive charge at pH 7.4 compared to hIAPP (+4 vs +3, respectively) and, therefore, has a greater electrostatic contribution to $\Delta G°_{part}$. The disparity derives from residue 18, which is histidine in hIAPP and arginine in rIAPP. Notably, the lipid affinity of hIAPP becomes much greater than rIAPP upon lowering of the pH to 5.5, at which His18 is expected to be protonated (Figure S1 of the Supporting Information). This indicates that the partitioning terms other than $\Delta G°_{qE}$ are more favorable for hIAPP than rIAPP. The greatest difference is likely in $\Delta G°_{fold}$, as hIAPP forms a more canonical α-helix upon binding to the membrane (Figure 2A). A second indication of the importance of electrostatic interactions is the maximum protein to lipid ratio (P/L) of IAPP on the bilayer, CT_{max}. Our fits indicate CT_{max} values of approximately 1/8 (Table 1). If IAPP is only bound to one face of the bilayer, this corresponds to a protein to lipid ratio of 1/4, a density at which a +4 charge on IAPP would be exactly neutralized by the lipid. Within aggregates, the P/L ratio is likely near this value, where the electrostatic repulsions between IAPP molecules are fully screened.

Favorable protein−protein interactions stabilize association of IAPP into α-helical aggregates. Despite equivalent
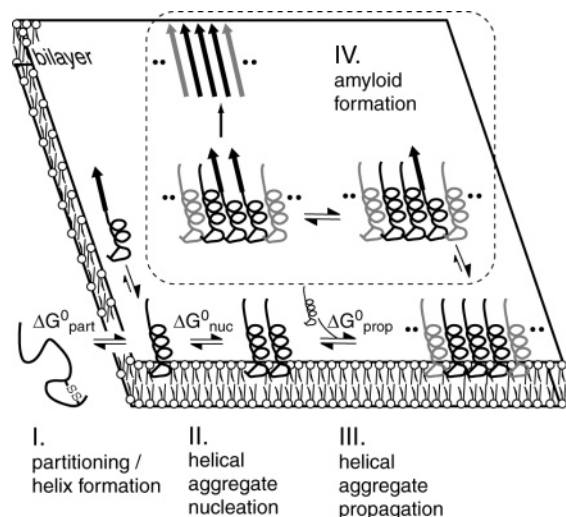
FIGURE 6: Model of IAPP−bilayer interactions. This model includes three steps in initial peptide−membrane interaction followed by a minutes time scale conversion of hIAPP to β-sheet amyloid fiber nuclei. (I) Binding of monomeric, random-coil IAPP to lipid and folding to α-helix is governed by a partitioning equilibrium (eq 14). (II) Aggregation of membrane-bound helical states is nucleated by formation of low-order aggregates [$\Delta G°_{nuc} = -RT \ln(\sigma s)$]. (III) Propagation of existing aggregates by addition of monomer is energetically more favorable than nucleation of new aggregates [$\Delta G°_{prop} = -RT \ln(s)$]. (IV) Aggregates of α-helical hIAPP, but not rIAPP, convert cooperatively to β-sheet fibers. This occurs via sampling of extended structures by molecules within the aggregate. Sampling of extended structure by free α-helical monomers (lower left) will less efficiently result in fiber nucleation.

monomer partitioning free energies, hIAPP shows greater apparent affinity for membrane compared to rIAPP; i.e., hIAPP has a more favorable $\Delta G_{IAPP−mem}$. This is evident from sucrose gradient centrifugation assays (*23*) as well as from CD titrations (Figure 2B,C). In this work, we have determined that both human and rodent sequences form α-helical aggregates as a result of favorable propagation free energies: $\Delta G°_{prop} = -3.1 \pm 0.1$ and -2.5 ± 0.1 kcal/mol, respectively (Table 1). The differences in $\Delta G°_{prop}$ are significant and result from differences in sequence and structure between the two variants. For small aggregates, the aggregation energy, ΔG_{Agg}, is significantly influenced by the nucleation term $\Delta G°_{nuc}$ (eq 15). For both hIAPP and rIAPP, this nucleation energy is higher than that of propagation, resulting in a cooperative aggregation process. This indicates that favorable protein−protein contacts are more readily formed during aggregate propagation. Differences between rIAPP and hIAPP propagation free energies may result from entropic and/or enthalpic factors which influence the stability of protein−protein interfaces. The relative significance of these contributions is dependent in part on the structures formed in the aggregated state.

Human and rat IAPP form α-helical structures of similar length when bound to membranes. Secondary structure prediction algorithms based solely on sequence predict α-helical structure in residues 8−14, which are identical between hIAPP and rIAPP (*52*). In addition, binding to membranes or detergents is known to induce α-helical structure in many peptides (*45*), and the helical region of IAPP likely extends beyond this predicted region when membrane-bound. Estimates of secondary structure based on CD measurements (Figure 2A) suggest 18−21 residue

helix lengths for both hIAPP and rIAPP. Figure 2A shows far-UV CD spectra of 20 μM peptide in the presence of 1.3 mM DOPG. At these concentrations, our model (Figure 2B,C) predicts that hIAPP and rIAPP are 69% and 51% bound, respectively. Since the spectra of unbound IAPP are known (Figure 2A, solid traces), we can deconvolute the measured spectra to yield the spectrum of 100% bound peptide (Figure 2A, thin dashes). This results in CD spectra that are more closely similar, particularly at the shorter 208 nm wavelength. Secondary structure estimation with these spectra suggests that rIAPP contains 49−57% helix and hIAPP contains 50−55% helix in the bound state.

Differences between the membrane-bound CD spectra of hIAPP and rIAPP may be ascribed to sequence differences. The unusually strong peak at 207 nm in rIAPP is reminiscent of the polyproline II helix (*33*). This suggests that the structured region includes one or more of the proline residues at positions 25, 28, and 29 (Figure 1). These prolines are extremely important in preventing β-sheet formation by rIAPP (*53*). Residues 28 and 29 are serine or proline in many IAPP sequences, and residue 30 is a conserved threonine (Figure 1A). These three residues are all poor helix formers (*54*) and may cap the C-terminal end of a conserved IAPP helix.

An α-helix formed by IAPP would have a conserved amphipathicity. This is a known property of other membrane-targeting peptides (*55*). A helical wheel representation of a 20 amino acid segment of the IAPP consensus sequence (residues 8−27) is shown in Figure 1B. The helix possesses a conserved hydrophobic moment of 4.8 $\pm$ 0.5. The disulfide-bonded loop region (residues 1−7) may cap the N-terminal end of the helix (*56*). Capping a helix with residues 1−7 places four positive charges very close in space. This occurs because Arg11 and Arg/His18 are on the same face of the helix as Cys7, near the charged N-terminus and Lys1. The negatively charged surface of the membrane can effectively screen these charges, allowing the helix to form. Interestingly, many sequences (notably in fish, Figure 1A) also contain an Asp at residue 14, one helical turn away from two positive charges, which would help to offset the charge repulsion. These features suggest a preference for α-helix formation in the phospholipid headgroup region of the membrane.

Aggregation of helices would necessitate a conformation of the peptide not parallel to the membrane surface. Indeed, the maximum allowed density of protein on the membrane (CT_{max}) is >2-fold higher than allowed by an α-helix lying on top of the bilayer. IAPP within the aggregates must therefore be partially inserted into the membrane and/or extended away from the surface. Fluorescence anisotropy measurements with rhodamine-labeled hIAPP suggest an orientation of the helix with the N-terminus partially inserted into the bilayer (Figure 6) (*23*). Such an orientation, which fixes only one terminus at the surface, will yield parallel rather than antiparallel helix−helix associations. Intriguingly, the hydrophobic face of the helix is consistent with a canonical coiled-coil interaction motif (Figure 1C) (*57*). Favorable coiled-coil interactions would be mediated by residues 12, 16, 23, and 26. Thus, the high density and amphipathicity of IAPP helices suggest that the helical aggregates are ordered parallel bundles.

The presence of α-helical aggregates of hIAPP accelerates conversion to β-sheet-rich amyloid fibers (Figure 4). Many amyloid fibers, including hIAPP (*7*), have been shown to contain β-sheets with parallel strand alignment (*5*, *8*, *58*). Parallel alignment of α-helices within an aggregate would all but eliminate translational and rotational diffusion on the membrane (Figure 6, step III). This would serve to accelerate fiber formation but competes with the adoption of a non-amyloid helical structure. Nevertheless, α-helical membrane-bound structures will sample helix−coil transitions (Figure 6, step IV). We therefore propose that aggregates containing both α and β structures give rise to a cooperative transition to amyloid (Figure 6, step IV).

We show that both amyloidogenic hIAPP and nonamyloidogenic rIAPP induce membrane leakage. We also note that in nonamyloidogenic peptide−membrane systems, e.g., melittin, multiple mechanisms of disruption are possible depending on the solution conditions (*59*). Under our conditions, IAPP is random coil in solution and α-helix on the membrane on the time scale of disruption. By contrast, other studies have used hIAPP prepared by dissolution of lyophilized peptide in unbuffered water or dilute HFIP (*11*, *60*). This is known to give rise to preassembled β-sheet structures rich in fibers and protofibers (*29*, *60*). These states are active on 100% zwitterionic (PC) membranes, whereas we observe no binding of IAPP to DOPC (*23*). Our interpretation of these studies is that aggregation is initiated in the aqueous phase, and β-sheet-rich oligomeric intermediates interact with membranes and cause disruption. Under our solution conditions, both hIAPP and rIAPP bind membranes from a random-coil state, likely monomeric, and disrupt via α-helical states at the interface. Previous studies report no leakage by rIAPP and equate β-sheet formation with toxicity (*9*, *40*, *50*, *51*). In vivo, it is not known whether β-sheet conversion precedes or follows membrane disruption by hIAPP. Our data suggest that α-helical aggregated states are sufficient to induce toxicity and may represent the toxic state of hIAPP.

β-cell apoptosis is observed much less frequently in diabetic rats than in humans (*61*). Similarly, we observe that 3−5-fold higher concentrations of rIAPP than hIAPP are necessary to induce cooperative membrane binding (Figure 2) or bilayer disruption (Figure 5). Furthermore, hIAPP binds membranes more tightly than rIAPP at secretory granule pH (Figure S1 of the Supporting Information). If increased IAPP−membrane binding occurs in diabetic islets, hIAPP will form aggregates more readily than rIAPP. Thus, the difference in helix aggregation propensity may be responsible for the dramatically different pathology observed in rodents and humans. Nevertheless, rare populations of rIAPP α-helical aggregates may account for the small increase in apoptosis in diabetic rodents (*18*). The lack of amyloid formation by rIAPP would therefore be unrelated to toxicity. Rather, it is solely attributable to the inability of rIAPP to form β-sheet structures (Figure 6, step IV).

The structures and mechanisms of IAPP−membrane interactions are similar between rIAPP and hIAPP and involve cooperative membrane binding as well as cooperative aggregation on the membrane (Figure 6). Helical analysis across 21 species shows a conserved amphipathicity and possibly an interaction motif (Figure 1). This high degree of conservation suggests that helical membrane binding represents an evolutionarily selected function. We have previously shown that 50 μM rIAPP partially binds to 3.6 mM of 1:1 DOPG:DOPC (*23*). This corresponds to an apparent K_d of ∼10 mM. While the anionic lipid content in vivo is ∼2-fold less than this, we estimate the effective lipid concentration for IAPP to be ∼50 mM (*1*).[3] Thus, extrapolation from our in vitro measurements to secretory granule conditions indicates that IAPP−lipid interactions are plausible. A thermodynamic extrapolation of this kind, while speculative, is not without precedent. For example, the peptide magainin specifically binds anionic membranes (*62*); however, transient interactions with zwitterionic membranes enabled its α-helical structure to be determined by NMR (*63*). Our data would indicate that a functional membrane-bound state of IAPP would be transient and involve structures which do not include helical aggregates. Further studies are needed to determine whether IAPP, like the amyloidogenic protein α-synuclein (*14*), may have a native function as a membrane binding protein.

SUPPORTING INFORMATION AVAILABLE

CD measurements of rIAPP and hIAPP binding to DOPG at pH 5.5 (Figure S1). This material is available free of charge via the Internet at http://pubs.acs.org.

REFERENCES

1. Hutton, J. C. (1989) The insulin secretory granule, *Diabetologia 32*, 271−281.
2. Hull, R. L., Westermark, G. T., Westermark, P., and Kahn, S. E. (2004) Islet amyloid: a critical entity in the pathogenesis of type 2 diabetes, *J. Clin. Endocrinol. Metab. 89*, 3629−3643.
3. Johnson, K. H., O'Brien, T. D., Hayden, D. W., Jordan, K., Ghobrial, H. K., Mahoney, W. C., and Westermark, P. (1988) Immunolocalization of islet amyloid polypeptide (IAPP) in pancreatic beta cells by means of peroxidase-antiperoxidase (PAP) and protein A-gold techniques, *Am. J. Pathol. 130*, 1−8.
4. Caughey, B., and Lansbury, P. T. (2003) Protofibrils, pores, fibrils, and neurodegeneration: separating the responsible protein aggregates from the innocent bystanders, *Annu. Rev. Neurosci. 26*, 267−298.
5. Nelson, R., Sawaya, M. R., Balbirnie, M., Madsen, A. O., Riekel, C., Grothe, R., and Eisenberg, D. (2005) Structure of the cross-beta spine of amyloid-like fibrils, *Nature 435*, 773−778.
6. Tycko, R. (2004) Progress towards a molecular-level structural understanding of amyloid fibrils, *Curr. Opin. Struct. Biol. 14*, 96−103.
7. Jayasinghe, S. A., and Langen, R. (2004) Identifying structural features of fibrillar islet amyloid polypeptide using site-directed spin labeling, *J. Biol. Chem. 279*, 48420−48425.
8. Benzinger, T. L., Gregory, D. M., Burkoth, T. S., Miller-Auer, H., Lynn, D. G., Botto, R. E., and Meredith, S. C. (2000) Two-dimensional structure of beta-amyloid(10−35) fibrils, *Biochemistry 39*, 3491−3499.
9. Janson, J., Ashley, R. H., Harrison, D., McIntyre, S., and Butler, P. C. (1999) The mechanism of islet amyloid polypeptide toxicity is membrane disruption by intermediate-sized toxic amyloid particles, *Diabetes 48*, 491−498.
10. Lesne, S., Koh, M. T., Kotilinek, L., Kayed, R., Glabe, C. G., Yang, A., Gallagher, M., and Ashe, K. H. (2006) A specific

amyloid-beta protein assembly in the brain impairs memory, *Nature 440*, 352−357.

11. Kayed, R., Sokolov, Y., Edmonds, B., McIntire, T. M., Milton, S. C., Hall, J. E., and Glabe, C. G. (2004) Permeabilization of lipid bilayers is a common conformation-dependent activity of soluble amyloid oligomers in protein misfolding diseases, *J. Biol. Chem. 279*, 46363−46366.

12. Ehehalt, R., Keller, P., Haass, C., Thiele, C., and Simons, K. (2003) Amyloidogenic processing of the Alzheimer beta-amyloid precursor protein depends on lipid rafts, *J. Cell Biol. 160*, 113−123.

13. Vey, M., Pilkuhn, S., Wille, H., Nixon, R., DeArmond, S. J., Smart, E. J., Anderson, R. G., Taraboulos, A., and Prusiner, S. B. (1996) Subcellular colocalization of the cellular and scrapie prion proteins in caveolae-like membranous domains, *Proc. Natl. Acad. Sci. U.S.A. 93*, 14945−14949.

14. Chandra, S., Gallardo, G., Fernandez-Chacon, R., Schluter, O. M., and Sudhof, T. C. (2005) Alpha-synuclein cooperates with CSPalpha in preventing neurodegeneration, *Cell 123*, 383−396.

15. Kahn, S. E., Andrikopoulos, S., and Verchere, C. B. (1999) Islet amyloid: a long-recognized but underappreciated pathological feature of type 2 diabetes, *Diabetes 48*, 241−253.

16. Tschop, M., and Heiman, M. L. (2001) Rodent obesity models: an overview, *Exp. Clin. Endocrinol. Diabetes 109*, 307−319.

17. Hoppener, J. W., Oosterwijk, C., Nieuwenhuis, M. G., Posthuma, G., Thijssen, J. H., Vroom, T. M., Ahren, B., and Lips, C. J. (1999) Extensive islet amyloid formation is induced by development of Type II diabetes mellitus and contributes to its progression: pathogenesis of diabetes in a mouse model, *Diabetologia 42*, 427−434.

18. Shimabukuro, M., Zhou, Y. T., Levi, M., and Unger, R. H. (1998) Fatty acid-induced beta cell apoptosis: a link between obesity and diabetes, *Proc. Natl. Acad. Sci. U.S.A. 95*, 2498−2502.

19. Efanova, I. B., Zaitsev, S. V., Zhivotovsky, B., Kohler, M., Efendic, S., Orrenius, S., and Berggren, P. O. (1998) Glucose and tolbutamide induce apoptosis in pancreatic beta-cells. A process dependent on intracellular Ca^{2+} concentration, *J. Biol. Chem. 273*, 33501−33507.

20. Poitout, V., and Robertson, R. P. (2002) Minireview: Secondary beta-cell failure in type 2 diabetes—a convergence of glucotoxicity and lipotoxicity, *Endocrinology 143*, 339−342.

21. Butler, A. E., Jang, J., Gurlo, T., Carty, M. D., Soeller, W. C., and Butler, P. C. (2004) Diabetes due to a progressive defect in beta-cell mass in rats transgenic for human islet amyloid polypeptide (HIP Rat): a new model for type 2 diabetes, *Diabetes 53*, 1509−1516.

22. Butler, A. E., Janson, J., Soeller, W. C., and Butler, P. C. (2003) Increased beta-cell apoptosis prevents adaptive increase in beta-cell mass in mouse model of type 2 diabetes: evidence for role of islet amyloid formation rather than direct action of amyloid, *Diabetes 52*, 2304−2314.

23. Knight, J. D., and Miranker, A. D. (2004) Phospholipid catalysis of diabetic amyloid assembly, *J. Mol. Biol. 341*, 1175−1187.

24. Rustenbeck, I., Matthies, A., and Lenzen, S. (1994) Lipid composition of glucose-stimulated pancreatic islets and insulin-secreting tumor cells, *Lipids 29*, 685−692.

25. Farese, R. V., DiMarco, P. E., Barnes, D. E., Sabir, M. A., Larson, R. E., Davis, J. S., and Morrison, A. D. (1986) Rapid glucose-dependent increases in phosphatidic acid and phosphoinositides in rat pancreatic islets, *Endocrinology 118*, 1498−1503.

26. Jayasinghe, S. A., and Langen, R. (2005) Lipid membranes modulate the structure of islet amyloid polypeptide, *Biochemistry 44*, 12113−12119.

27. Terzi, E., Holzemann, G., and Seelig, J. (1997) Interaction of Alzheimer beta-amyloid peptide(1−40) with lipid membranes, *Biochemistry 36*, 14845−14852.

28. Jo, E., McLaurin, J., Yip, C. M., St George-Hyslop, P., and Fraser, P. E. (2000) alpha-Synuclein membrane interactions and lipid specificity, *J. Biol. Chem. 275*, 34328−34334.

29. Padrick, S. B., and Miranker, A. D. (2002) Islet amyloid: phase partitioning and secondary nucleation are central to the mechanism of fibrillogenesis, *Biochemistry 41*, 4694−4703.

30. Munishkina, L. A., Phelan, C., Uversky, V. N., and Fink, A. L. (2003) Conformational behavior and aggregation of alpha-synuclein in organic solvents: modeling the effects of membranes, *Biochemistry 42*, 2720−2730.

31. Fezoui, Y., and Teplow, D. B. (2002) Kinetic studies of amyloid beta-protein fibril assembly. Differential effects of alpha-helix stabilization, *J. Biol. Chem. 277*, 36948−36954.

32. Kirkitadze, M. D., Condron, M. M., and Teplow, D. B. (2001) Identification and characterization of key kinetic intermediates in amyloid beta-protein fibrillogenesis, *J. Mol. Biol. 312*, 1103−1119.

33. Greenfield, N. J. (2004) Analysis of circular dichroism data, *Methods Enzymol. 383*, 282−317.

34. Sreerama, N., and Woody, R. W. (2000) Estimation of protein secondary structure from circular dichroism spectra: comparison of CONTIN, SELCON, and CDSSTR methods with an expanded reference set, *Anal. Biochem. 287*, 252−260.

35. Sreerama, N., and Woody, R. W. (2004) On the analysis of membrane protein circular dichroism spectra, *Protein Sci. 13*, 100−112.

36. Terzi, E., Holzemann, G., and Seelig, J. (1995) Self-association of beta-amyloid peptide (1−40) in solution and binding to lipid membranes, *J. Mol. Biol. 252*, 633−642.

37. Wimley, W. C., Hristova, K., Ladokhin, A. S., Silvestro, L., Axelsen, P. H., and White, S. H. (1998) Folding of beta-sheet membrane proteins: a hydrophobic hexapeptide model, *J. Mol. Biol. 277*, 1091−1110.

38. Schagger, H., and von Jagow, G. (1987) Tricine-sodium dodecyl sulfate-polyacrylamide gel electrophoresis for the separation of proteins in the range from 1 to 100 kDa, *Anal. Biochem. 166*, 368−379.

39. Wensel, T. G., He, F., and Malinski, J. A. (2005) Purification, reconstitution on lipid vesicles, and assays of PDE6 and its activator G protein, transducin, *Methods Mol. Biol. 307*, 289−313.

40. Green, J. D., Kreplak, L., Goldsbury, C., Li Blatter, X., Stolz, M., Cooper, G. S., Seelig, A., Kistler, J., and Aebi, U. (2004) Atomic force microscopy reveals defects within mica supported lipid bilayers induced by the amyloidogenic human amylin peptide, *J. Mol. Biol. 342*, 877−887.

41. Tamba, Y., and Yamazaki, M. (2005) Single giant unilamellar vesicle method reveals effect of antimicrobial peptide magainin 2 on membrane permeability, *Biochemistry 44*, 15823−15833.

42. Chang, C. L., Roh, J., and Hsu, S. Y. (2004) Intermedin, a novel calcitonin family peptide that exists in teleosts as well as in mammals: a comparison with other calcitonin/intermedin family peptides in vertebrates, *Peptides 25*, 1633−1642.

43. Brown, N. P., Leroy, C., and Sander, C. (1998) MView: a web-compatible database search or multiple alignment viewer, *Bioinformatics 14*, 380−381.

44. Jayasinghe, S. A., Hristova, K., and White, S. H. (2000) http://blanco.biomol.uci.edu/mpex.

45. White, S. H., and Wimley, W. C. (1999) Membrane protein folding and stability: physical principles, *Annu. Rev. Biophys. Biomol. Struct. 28*, 319−365.

46. Kurganov, B., Doh, M., and Arispe, N. (2004) Aggregation of liposomes induced by the toxic peptides Alzheimer's Abetas, human amylin and prion (106−126): facilitation by membrane-bound GM1 ganglioside, *Peptides 25*, 217−232.

47. Habeeb, A. J., and Hiramoto, R. (1968) Reaction of proteins with glutaraldehyde, *Arch. Biochem. Biophys. 126*, 16−26.

48. Padrick, S. B., and Miranker, A. D. (2001) Islet amyloid polypeptide: identification of long-range contacts and local order on the fibrillogenesis pathway, *J. Mol. Biol. 308*, 783−794.

49. Ferrone, F. (1999) Analysis of protein aggregation kinetics, *Methods Enzymol. 309*, 256−274.

50. Mirzabekov, T. A., Lin, M. C., and Kagan, B. L. (1996) Pore formation by the cytotoxic islet amyloid peptide amylin, *J. Biol. Chem. 271*, 1988−1992.

51. Sparr, E., Engel, M. F., Sakharov, D. V., Sprong, M., Jacobs, J., de Kruijff, B., Hoppener, J. W., and Killian, J. A. (2004) Islet amyloid polypeptide-induced membrane leakage involves uptake of lipids by forming amyloid fibers, *FEBS Lett. 577*, 117−120.

52. Jaikaran, E. T., Higham, C. E., Serpell, L. C., Zurdo, J., Gross, M., Clark, A., and Fraser, P. E. (2001) Identification of a novel human islet amyloid polypeptide beta-sheet domain and factors influencing fibrillogenesis, *J. Mol. Biol. 308*, 515−525.

53. Westermark, P., Engstrom, U., Johnson, K. H., Westermark, G. T., and Betsholtz, C. (1990) Islet amyloid polypeptide: pinpointing amino acid residues linked to amyloid fibril formation, *Proc. Natl. Acad. Sci. U.S.A. 87*, 5036−5040.

54. Chou, P. Y., and Fasman, G. D. (1974) Prediction of protein conformation, *Biochemistry 13*, 222−245.

55. Eisenberg, D., Schwarz, E., Komaromy, M., and Wall, R. (1984) Analysis of membrane and surface protein sequences with the hydrophobic moment plot, *J. Mol. Biol. 179*, 125−142.

56. Breeze, A. L., Harvey, T. S., Bazzo, R., and Campbell, I. D. (1991) Solution structure of human calcitonin gene-related peptide by ^{1}H NMR and distance geometry with restrained molecular dynamics, *Biochemistry 30*, 575−582.

57. Cohen, C., and Parry, D. A. (1990) Alpha-helical coiled coils and bundles: how to design an alpha-helical protein, *Proteins 7*, 1−15.

58. Antzutkin, O. N., Balbach, J. J., Leapman, R. D., Rizzo, N. W., Reed, J., and Tycko, R. (2000) Multiple quantum solid-state NMR indicates a parallel, not antiparallel, organization of beta-sheets in Alzheimer's beta-amyloid fibrils, *Proc. Natl. Acad. Sci. U.S.A. 97*, 13045−13050.

59. Ladokhin, A. S., and White, S. H. (2001) "Detergent-like" permeabilization of anionic lipid vesicles by melittin, *Biochim. Biophys. Acta 1514*, 253−260.

60. Quist, A., Doudevski, I., Lin, H., Azimova, R., Ng, D., Frangione, B., Kagan, B., Ghiso, J., and Lal, R. (2005) Amyloid ion channels: a common structural link for protein-misfolding disease, *Proc. Natl. Acad. Sci. U.S.A. 102*, 10427−10432.

61. Lingohr, M. K., Buettner, R., and Rhodes, C. J. (2002) Pancreatic beta-cell growth and survival—a role in obesity-linked type 2 diabetes?, *Trends Mol. Med. 8*, 375−384.

62. Matsuzaki, K., Sugishita, K., Fujii, N., and Miyajima, K. (1995) Molecular basis for membrane selectivity of an antimicrobial peptide, magainin 2, *Biochemistry 34*, 3423−3429.

63. Wakamatsu, K., Takeda, A., Tachi, T., and Matsuzaki, K. (2002) Dimer structure of magainin 2 bound to phospholipid vesicles, *Biopolymers 64*, 314−327.